Orientational Ordering in Athermally Sheared, Aspherical, Frictionless Particles

Theodore Marschall,[1] Yann-Edwin Keta,[2,3,4] Peter Olsson,[2] and S. Teitel[1]

[1] *Department of Physics and Astronomy, University of Rochester, Rochester, NY 14627*
[2] *Department of Physics, Umeå University, 901 87 Umeå, Sweden*
[3] *Département de Physique, École Normale Supérieure de Lyon, 69364 Lyon Cedex 07, France*
[4] *Département de Physique, Université Claude Bernard Lyon 1, 69622 Villeurbanne Cedex, France*

(Dated: June 6, 2018)

We numerically simulate the uniform athermal shearing of bidisperse, frictionless, two dimensional spherocylinders and three dimensional prolate ellipsoids. We focus on the orientational ordering of the particles, considering behavior as an asphericity parameter $\alpha \to 0$ and particles approach spherical. We find that the nematic order parameter S_2 is a non-monotonic function of packing fraction ϕ, with a peak height $S_{2\,\max}$ that remains large even for quite small α. In the $\alpha \to 0$ limit we find that $S_{2\,\max}$ stays finite. Particle contacts are found to preferentially lie along the narrowest width of the particles, even as $\alpha \to 0$. The approach to spherical particles thus appears to be singular.

When a particle is placed in a uniform shear flow, drag forces between the particle and the flow will cause the particle to tumble [1]. If the particle is asymmetrical, with unequal eigenvalues of its moment of inertia tensor, tumbling will have a non-uniform rotational velocity; the torque from drag forces will vary with the particle's orientation particle, and the particle will on average align with the flow direction. For a finite density of colliding particles, this nematic ordering remains but the nematic director becomes oriented at a finite angle with respect to the flow direction [2–8].

Here we investigate the nematic ordering of frictionless, aspherically shaped particles, athermally sheared at a constant shear strain rate $\dot\gamma$. We consider the behavior as an asphericity parameter $\alpha \to 0$, and the particles approach spherical. We find several surprising results: (i) nematic ordering varies non-monotonically as particle density increases, (ii) finite nematic ordering persists even as $\alpha \to 0$; (iii) for $\alpha \to 0$ near jamming and above, particle contacts show a marked preference to be located where the particles are narrowest. We find these results within two quite different model systems, thus suggesting that these behaviors are robust features of shear driven aspherical particles. Our results suggest that the shear driven jamming of aspherical particles has a singular limit as $\alpha \to 0$. Since most particles in nature are not truly spherical, our result may have broad implications for granular shear flows.

Models: We consider two different numerical models: (i) spherocylinders in two dimensions (2D), and (ii) prolate ellipsoids in three dimensions (3D). In both cases we take a bidisperse distribution of particle sizes, with equal numbers of big and small particles with a ratio of length scales of 1.4. We use soft-core particles with a one-sided harmonic elastic repulsion. We use a system of length $\mathcal{L}$ in all directions, with periodic boundary conditions along the flow direction $\hat{\mathbf{x}}$, and apply a uniform shear flow by using Lees-Edwards boundary conditions [9] with a uniform shear strain rate $\dot\gamma$ in the transverse direction $\hat{\mathbf{y}}$. For our 3D system we take periodic boundary conditions along the direction of the average vorticity $\hat{\mathbf{z}}$. The particle packing fraction is $\phi = \sum_i v_i/\mathcal{V}$, where v_i is the volume of particle i and $\mathcal{V} = \mathcal{L}^d$ is the volume of the system, with $d = 2$ or 3 for 2D and 3D respectively.

2D Spherocylinders: A spherocylinder in 2D consists of a rectangle of length L, with two semi-circular end caps of diameter D, as illustrated in the inset to Fig. 5a. We define the asphericity parameter as $\alpha = L/D$. Big and small particles have equal α, with $D_b/D_s = 1.4$. Taking the "spine" of the spherocylinder as the line that bisects the rectangle parallel to its length L, we define r_{ij} as the shortest distance between the spines of spherocylinders i and j and $d_{ij} = (D_i + D_j)/2$. Two spherocylinders are then in contact whenever $r_{ij} < d_{ij}$, in which case the elastic interaction is $U^{\rm el} = (k_e/2)(1 - r_{ij}/d_{ij})^2$ and the resulting repulsive elastic force on i is $\mathbf{F}^{\rm el}_{ij} = (k_e/d_{ij})(1 - r_{ij}/d_{ij})\hat{\mathbf{n}}_{ij}$, where $\hat{\mathbf{n}}_{ij}$ is a unit vector pointing normally inwards to particle i at the point of contact with particle j and k_e sets the energy scale [10].

Our dynamical model is a generalization to non-spherical particles of the mean-field Durian model for foams [11]. We model the dissipative force on a spherocylinder to be a Stokes drag between the particle and a uniform background shear flow, $\mathbf{F}^{\rm dis}_i = -k_d v_i(\dot{\mathbf{r}}_i - y_i\dot\gamma\hat{\mathbf{x}})$, where $\mathbf{r}_i = (x_i, y_i)$ is the center of mass of spherocylinder i, $\dot{\mathbf{r}}_i$ the center of mass velocity, and k_d the viscous coupling. We use an overdamped dynamics $\mathbf{F}^{\rm dis}_i + \sum_j \mathbf{F}^{\rm el}_{ij} = 0$, where the sum is over all particles j in contact with i.

The elastic and dissipative forces produce torques on the spherocylinders that determine the rotational motion. The elastic torque on particle i due to contact with j is, $\boldsymbol{\tau}^{\rm el}_{ij} = \hat{\mathbf{z}}\tau^{\rm el}_{ij} = \mathbf{s}_{ij} \times \mathbf{F}^{\rm el}_{ij}$, where $\mathbf{s}_{ij}$ is the moment arm from the center of mass of spherocylinder i to its point of contact with j. A dissipative torque arises because of the variation of the background shear flow velocity over the spatial extent of the particle [12]. Integrating over the particle area one gets $\tau^{\rm dis}_i = -k_d v_i I_i[\dot\theta_i + \dot\gamma f(\theta_i)]$, where θ_i is the angle of the spherocylinder spine with respect to the flow direction $\hat{\mathbf{x}}$, and $f(\theta) = [1 - C\cos 2\theta]/2$. The overdamped $\tau^{\rm dis}_i + \sum_j \tau^{\rm el}_{ij} = 0$ then determines the rotation of the particles. Here I_i is the sum of the two eigenvalues of the

moment of inertia tensor, and $C = \Delta I_i/I_i$, where ΔI_i is the difference between the two eigenvalues. For spherocyliners, $I_i = (D_i/2)^2(3\pi + 24\alpha + 6\pi\alpha^2 + 8\alpha^3)/(6\pi + 24\alpha)$. For a circle, $\Delta I = 0$, and in the absence of collisions one has $\dot\theta/\dot\gamma = -1/2$. We take the unit of length to be $D_s = 1$, the unit of energy to be $k_e = 1$, and the unit of time to be $t_0 = D_s^2 k_d/k_e = 1$. We integrate the equations of motion using the Heun method with a step size $\Delta t/t_0 = 0.02$. We use $N = 1024$ particles.

3D Prolate Ellipsoids: We take prolate ellipsoids of revolution with major axis of length a_1 and minor axes of length a_2. We define the asphericity parameter as $\alpha = a_1/a_2 - 1$. Big and small particles have equal α, with $a_{1b}/a_{1s} = 1.4$. For two ellipsoids i and j that overlap, we define a scale factor $\delta_{ij} < 1$ such that the particles just barely touch when their axes are rescaled by δ_{ij}. Note, δ_{ij} depends on the relative orientations of the two ellipsoids. The elastic interaction is then $U^{\rm el} = (k_e/2)(1-\delta_{ij})^2$, and the corresponding repulsive elastic force on i is $\mathbf{F}_{ij}^{\rm el} = k_e\delta_{ij}(1-\delta_{ij})\hat{\mathbf{n}}_{ij}/[(\mathbf{r}_i - \mathbf{r}_j)\cdot\hat{\mathbf{n}}_{ij}]$, where $\mathbf{r}_i$ is the center of mass of ellipsoid i and $\hat{\mathbf{n}}_{ij}$ is a unit vector pointing normally inwards to particle i at the point of contact with particle j [13].

We take a purely collisional dynamics, where the dissipative force on ellipsoid i is due to contact with ellipsoid j and is proportional to the difference in particle velocities at their point of contact, $\mathbf{F}_{ij}^{\rm dis} = -k_d(\dot{\mathbf{r}}_i + \boldsymbol{\omega}_i \times \mathbf{s}_{ij} - \dot{\mathbf{r}}_j - \boldsymbol{\omega}_j \times \mathbf{s}_{ji})$, where $\dot{\mathbf{r}}_i$ is the center of mass velocity, $\boldsymbol{\omega}_i$ is the angular velocity about the center of mass, and $\mathbf{s}_{ij}$ is the moment arm from the center of ellipsoid i to the point of contact with j [14]. We use Newton's equation of motion for inertial particles, $m_i\ddot{\mathbf{r}}_i = \sum_j[\mathbf{F}_{ij}^{\rm dis} + \mathbf{F}_{ij}^{\rm el}]$, where the sum is over all particles j in contact with i, and m_i is the mass of ellipsoid i. We take mass m_i proportional to particle volume v_i. The elastic and dissipative forces give rise to torques on the ellipsoids, and the rotation of particle i is governed by, $\mathbf{I}_i \cdot \dot{\boldsymbol{\omega}}_i = \sum_j \mathbf{s}_{ij} \times [\mathbf{F}_{ij}^{\rm dis} + \mathbf{F}_{ij}^{\rm el}]$, where $\mathbf{I}_i$ is the moment of inertia tensor of ellipsoid i.

We take the unit of length to be $D_s \equiv \sqrt[3]{a_{1s}a_{2s}^2} = 1$, the unit of energy to be $k_e = 1$, the unit of mass to be $m_s = 1$ and the unit of time to be $t_0 = D_s\sqrt{m_s/k_e} = 1$. The elasticity of collisions is measured by $Q = \sqrt{m_s k_e}/(k_d D_s) = 2$, which would be the quality factor if the interaction was viewed as a damped oscillator. We integrate the equations of motion using a modified velocity Verlet algorithm [14] with a step size $\Delta t/t_0 = 0.05$. We use $N = 1024$ particles.

Results: In this work we focus on the tumbling and orientational order of particles, rather than their rheology. To determine the nematic ordering we compute the average orientational ordering tensor [5],

$$\langle T_{\mu\nu}\rangle = \left\langle \frac{d}{(d-1)N}\sum_{i=1}^{N}\left[\hat\ell_{i\mu}\hat\ell_{i\nu} - \frac{1}{d}\delta_{\mu\nu}\right]\right\rangle \qquad (1)$$

where $\hat{\boldsymbol{\ell}}_i$ is a unit vector lying along the spine of the spherocylinder or the major axis of the ellipsoid, μ and ν denote components in the different spatial directions, $d = 2, 3$ is the spatial dimension, and $\langle \dots \rangle$ denotes an average over configurations in the sheared ensemble. The largest eigenvalue of $\langle T_{\mu\nu}\rangle$ is the magnitude of the nematic order parameter S_2, and the corresponding eigenvector $\hat{\boldsymbol{\ell}}_2$ gives the orientation of the nematic director, which by symmetry must lie in the xy plane. We define θ_2 as the angle that $\hat{\boldsymbol{\ell}}_2$ makes with respect to the flow direction $\hat{\mathbf{x}}$, and define $\mathbf{S}_2 = S_2\hat{\boldsymbol{\ell}}_2$.

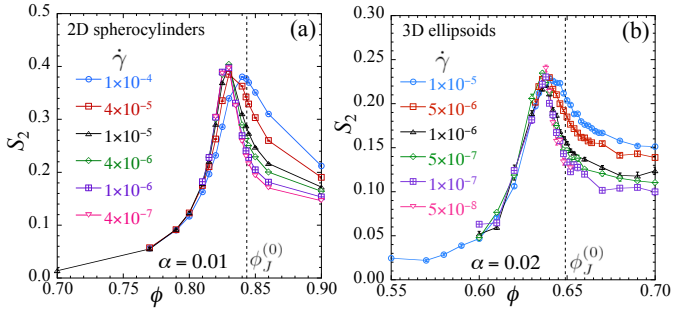

FIG. 1. Nematic order parameter S_2 vs packing fraction ϕ at different shear strain rates $\dot\gamma$. (a) 2D spherocylinders at asphericity $\alpha = 0.01$, (b) 3D ellipsoids at $\alpha = 0.02$. Vertical dashed lines locate the jamming transition of $\alpha = 0$ spherical particles, $\phi_J^{(0)} = 0.8433$ for 2D [15–17] and 0.649 for 3D [18].

In Fig. 1 we plot S_2 vs packing fraction ϕ for particles of fixed small asphericity α, at different shear rates $\dot\gamma$. Fig. 1a shows 2D spherocylinders at $\alpha = 0.01$, while Fig. 1b shows 3D ellipsoids at $\alpha = 0.02$. In both cases we see similar behavior. In contrast to previous works [2–4] that found orientational order increased with increasing ϕ, here we find that, upon increasing ϕ further into the dense region approaching and above jamming, S_2 is non-monotonic with a peak value $S_{2\,\rm max}$ occurring at a $\phi_{\rm max}$ that lies slightly below the $\alpha = 0$ jamming transition at $\phi_J^{(0)}$. As $\dot\gamma$ decreases, the values of S_2 approach a common limiting curve [5, 6], but the $\dot\gamma$ dependence is stronger on the denser side of the peak, $\phi > \phi_{\rm max}$.

In Fig. 2 we plot S_2 vs ϕ for a range of asphericities α, showing results for both a smaller $\dot\gamma_1$ (solid symbols) and a larger $\dot\gamma_2$ (open symbols); see Table I for values. In each case $\dot\gamma_1$ and $\dot\gamma_2$ are sufficiently small that S_2 shows no noticeable $\dot\gamma$ dependence for ϕ up to and slightly beyond the peak at $\phi_{\rm max}$, however some small $\dot\gamma$ dependence remains at the highest ϕ. What is remarkable is that the orientational ordering $S_{2\,\rm max}$ remains quite sizable even for particles very close to spherical with $\alpha = 0.001$.

TABLE I. Strain rate values used for data in Figs. 2 and 3

2D: α	$\dot\gamma_1$	$\dot\gamma_2$	3D: α	$\dot\gamma_1$	$\dot\gamma_2$
0.001	1×10^{-7}	4×10^{-7}	$\alpha \le 0.02$	1×10^{-7}	2×10^{-7}
0.01	4×10^{-7}	1×10^{-6}	0.05	5×10^{-7}	1×10^{-6}
$\alpha \ge 0.06$	1×10^{-5}	4×10^{-5}	0.2	2×10^{-6}	5×10^{-6}
			0.7	5×10^{-6}	1×10^{-5}

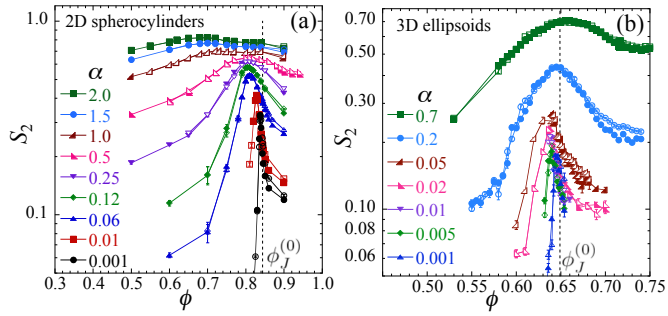

FIG. 2. Nematic order parameter S_2 for (a) 2D spherocylinders and (b) 3D ellipsoids vs packing fraction ϕ for different particle asphericities α. For each α we show results for two different strain rates $\dot\gamma_1$ (solid symbols) $< \dot\gamma_2$ (open symbols), see Table I for values. Vertical dashed lines locate the jamming transition $\phi_J^{(0)}$ of $\alpha = 0$ spherical particles.

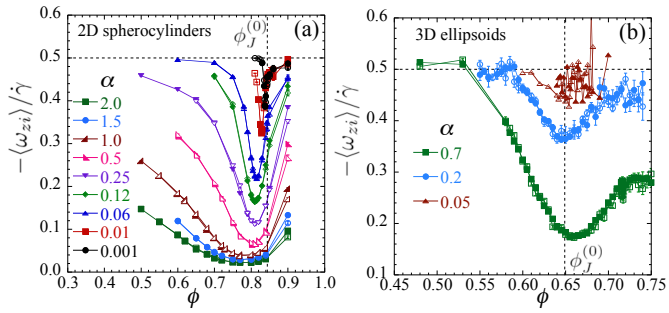

FIG. 3. Component of average particle angular velocity in the direction of the system vorticity, scaled by strain rate, $-\langle\omega_{zi}\rangle/\dot\gamma$ for (a) 2D spherocylinders and (b) 3D ellipsoids vs packing fraction ϕ for different particle asphericities α. For each α we show results for two different strain rates $\dot\gamma_1$ (solid symbols) $< \dot\gamma_2$ (open symbols), see Table I for values. Vertical dashed lines locate the jamming transition $\phi_J^{(0)}$ of $\alpha = 0$ spherical particles. Spherical particles rotate with $-\langle\omega_{zi}\rangle/\dot\gamma = 1/2$.

The data in Fig. 2 represent the value of S_2 averaged over the steady state shearing ensemble. We have also looked at the instantaneous values of $S_2(\gamma)$ and $\theta_2(\gamma)$ as a function of the system strain $\gamma = \dot\gamma t$. We find that, everywhere near and above the peak at $\phi_{\rm max}$, $\mathbf{S}_2(\gamma)$ shows only random fluctuations about a well defined average; there is no macroscopically coherent tumbling of particles [19]. Given this observation, one can ask if individual particles still tumble incoherently [6, 7], or whether they are orientationally locked into small fluctuations about the orientation θ_2 of the nematic director $\hat{\boldsymbol{\ell}}_2$. We find the former to be the case.

In Fig. 3 we plot the component of the average particle angular velocity in the direction of the system vorticity, scaled by the strain rate, $-\langle\omega_{zi}\rangle/\dot\gamma$; note, $-\langle\omega_{zi}\rangle > 0$ indicates clockwise rotating particles. For 2D spherocylinders, $\omega_{zi} = \dot\theta_i$. In each case we show results at two different strain rates $\dot\gamma_1 < \dot\gamma_2$, as in Fig. 2 (see Table I), and find little dependence on $\dot\gamma$ except for the largest ϕ.

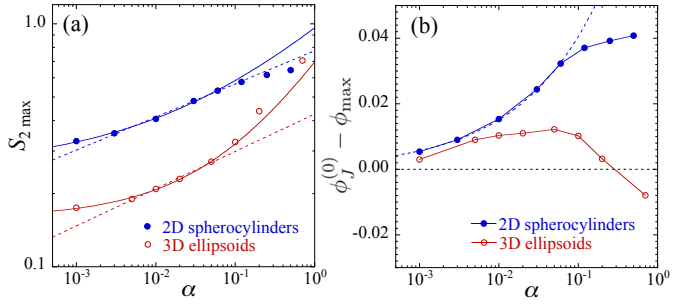

FIG. 4. For 2D spherocylinders and 3D ellipsoids: (a) $S_{2\,\rm max}$ vs α. Solid lines are fits to the empirical form $S_0 + c\alpha^\beta$, using the five smallest α points. Dropping the data point at $\alpha = 0.001$, dashed lines show fits to a pure power law. (b) $\phi_J^{(0)} - \phi_{\rm max}$ vs α, with $\phi_J^{(0)}$ the $\alpha = 0$ jamming point. We use $\phi_J^{(0)} = 0.8433$ for 2D spherocylinders [15–17] and 0.649 for 3D ellipsoids [18]. Solid lines connect the data points; dashed line for the 2D spherocylinders is a power law fit to the five smallest α points.

Comparing Figs. 2 and 3 we find that rotation velocity is anti-correlated with orientational order; $-\langle\omega_{zi}\rangle/\dot\gamma$ is non-monotonic in ϕ and is smallest when S_2 is largest. For spherical particles one has $-\langle\omega_{zi}\rangle/\dot\gamma = 1/2$ at all ϕ. For small but finite α, however, we see that $-\langle\omega_{zi}\rangle/\dot\gamma$ approaches $1/2$ at small ϕ, but shows a significant dip below $1/2$ at $\phi_{\rm max}$. For 2D spherocylinders, Fig. 3a shows that this dip remains sizable even for very small $\alpha = 0.001$. For 3D ellipsoids, we are unable to get accurate results down to similar small values of α, but Fig. 3b shows that the trends appear to be the same.

Returning to the behavior of the nematic order parameter, in Fig. 4a we plot $S_{2\,\rm max}$ vs α for both 2D spherocylinders and 3D ellipsoids. Solid lines are fits to the empirical form $S_{2\,\rm max} = S_0 + c\alpha^\beta$, using the five smallest α points. We find $S_0 = 0.25$ for 2D spherocylinders and $S_0 = 0.16$ for 3D ellipsoids. If we exclude the data point at the smallest $\alpha = 0.001$, then our data would be reasonably fit (dashed lines in Fig. 4a) by a pure power law with exponent ~ 0.14. However, in [19] we give detailed tests confirming that our data point at $\alpha = 0.001$ is accurate and so should not be excluded. We thus conclude that a finite orientational order persists even as $\alpha \to 0$, and hence the limit of approaching spherical particles is discontinuous.

In Fig. 4b we plot $\phi_J^{(0)} - \phi_{\rm max}$ vs α, where $\phi_J^{(0)}$ is the jamming density for spherical particles at $\alpha = 0$. For both 2D and 3D particles we find $\phi_J^{(0)} - \phi_{\rm max} \to 0$ as $\alpha \to 0$, thus showing that the peak in S_2 approaches the jamming transition as $\alpha \to 0$. For the 2D spherocylinders we find a power law dependence, $\phi_J^{(0)} - \phi_{\rm max} \sim \alpha^\Delta$ with $\Delta = 0.43$, as illustrated by the dashed line in the figure. For 3D ellipsoids, our data does not suggest any clear form for the small α behavior.

To look for a microscopic signature of this singular $\alpha \to 0$ limit, we consider the location on a particle's

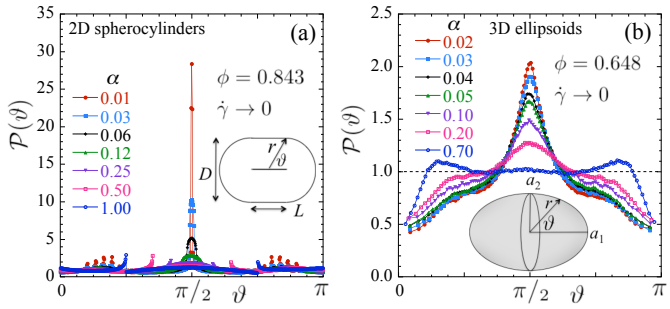

FIG. 5. Probability $\mathcal{P}(\vartheta)$ for a particle to have a contact at polar angle ϑ on its surface, for several different asphericities α at fixed ϕ near $\phi_J^{(0)}$: (a) 2D spherocylinders at $\phi = 0.843$ and (b) 3D ellipsoids at $\phi = 0.648$. Results are in the $\dot\gamma \to 0$ limit where $\mathcal{P}(\vartheta)$ becomes independent of $\dot\gamma$. Dashed lines represent the flat distribution for a spherical particle. In (a) the features and sharp peaks near $\vartheta = \pi/6$ and $5\pi/6$ are shadow effects from particles in contact exactly at $\vartheta = \pi/2$.

.

surface of the inter-particle contacts. For 2D spherocylinders we define (r, ϑ) as the radial distance and polar angle of a point on the surface with respect to the center of the particle and the direction of the spine. We define $\mathcal{P}(\vartheta)$ as the probability density per unit surface length to find a contact at ϑ, with normalization so that $1 = \mathcal{A}^{-1} \int_0^{2\pi} d\vartheta \sqrt{r^2 + (dr/d\vartheta)^2}\, \mathcal{P}(\vartheta)$, where $\mathcal{A}$ is the perimeter length of the particle [20]. For 3D ellipsoids, we define (r, ϑ, φ) as the spherical coordinates with respect to the major axis; $\mathcal{P}(\vartheta, \varphi)$ is the probability density per unit surface area to have a contact on the surface at (ϑ, φ), with normalization so that $1 = \mathcal{A}^{-1} \int_0^{2\pi} d\varphi \int_0^{\pi} d\vartheta \sin\vartheta\, r\sqrt{r^2 + (dr/d\vartheta)^2}\, \mathcal{P}(\vartheta, \varphi)$; $\mathcal{A}$ is the surface area. For simplicity we consider $\mathcal{P}(\vartheta) = (2\pi)^{-1} \int_0^{2\pi} d\varphi \mathcal{P}(\vartheta, \varphi)$. Angles are measured with respect to axes that are fixed on each particle, so that the axes tumble with the particle. For a uniform probability per unit surface area, such as would be for spherical particles, $\mathcal{P}(\vartheta) = 1$ in both 2D and 3D.

In Fig. 5 we plot $\mathcal{P}(\vartheta)$ vs ϑ for different values of α at fixed ϕ near $\phi_J^{(0)}$. For each α, $\mathcal{P}(\vartheta)$ also depends on the strain rate $\dot\gamma$, however as $\dot\gamma \to 0$ we find that $\mathcal{P}(\vartheta)$ approaches a limiting distribution. Our results in Fig. 5 are in this small $\dot\gamma$ limit (we exclude our smallest α results from this figure because for the smallest α we have not reached the $\dot\gamma \to 0$ limit for $\mathcal{P}(\vartheta)$). Unlike the uniform distribution expected for spheres, we see a sharp peak at $\vartheta = \pi/2$. As α decreases, the height of this peak steadily increases. Thus as α decreases, and particles become increasingly spherical, particle contacts increasingly prefer to form along the narrowest width of the particle rather than uniformly over the particle's surface [21]. Similar results have previously been reported in static, mechanically stable, jammed packings [10, 22].

Finally, in Fig. 6 we plot $\mathcal{P}(\pi/2)$ vs ϕ at fixed small α, for different values of $\dot\gamma$. We see that as $\dot\gamma$ decreases,

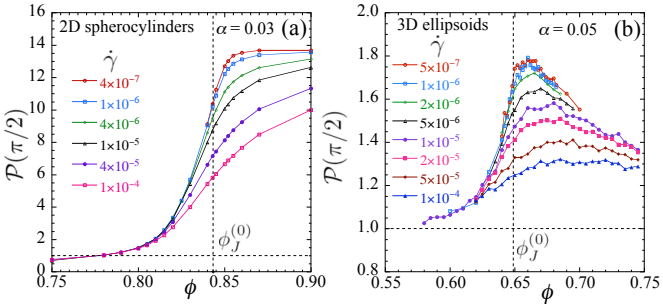

FIG. 6. Peak probability $\mathcal{P}(\pi/2)$ vs ϕ for different strain rates $\dot\gamma$ for (a) 2D spherocylinders at $\alpha = 0.03$ and (b) 3D ellipsoids at $\alpha = 0.05$. As $\dot\gamma$ decreases, the peak value $\mathcal{P}(\pi/2)$ increases until it saturates. Vertical dashed lines denote $\phi_J^{(0)}$, while horizontal dashed lines indicate the value of unity for a spherical particle.

$\mathcal{P}(\pi/2)$ increases to a limiting curve, which rises rapidly as ϕ approaches $\phi_J^{(0)}$, and then stays above the spherical particle value as ϕ increases above the jamming transition.

To conclude, we have considered the athermal uniform shearing of bidisperse, aspherical particles in two and three dimensions, studying the orientational ordering with particular attention to the limit where particle asphericity $\alpha \to 0$. We find that this limit is singular; the nematic order parameter S_2 is non-monotonic as a function of packing fraction ϕ, with a peak height $S_{2\,\max}$ that stays finite as $\alpha \to 0$. As $\alpha \to 0$, the region where $S_2 > 0$ becomes confined to the region of the jamming transition and above. Looking at microscopic configurations we find that, whereas perfectly spherical particles would have contacts distributed uniformly over their surface, contacts on aspherical particles as $\alpha \to 0$ increasingly prefer to form along the narrowest widths of the particles: i.e., along the flat sides for 2D spherocyliners, even though those flat sides comprise a vanishing fraction of the perimeter; and along the minor axes for 3D ellipsoids, even though the difference between minor and major axes lengths is shrinking to zero. We leave the question of what effects this singular $\alpha \to 0$ behavior might have on system rheology to future investigation.

Simulations were were carried out on resources at the Center for Integrated Research Computing at the University of Rochester and at the Swedish National Infrastructure for Computing (SNIC) at HPC2N.

[1] G. B. Jeffery, "The Motion of Ellipsoidal Particles Immersed in a Viscous Fluid," Proc. R. Soc. A **102**, 161 (1922).

[2] C. S. Campbell, "Elastic Granular Flows of Ellipsoidal Particles," Physics of Fluids **23**, 013306 (2011).

[3] Y. Guo, C. Wassgren, W. Ketterhagen, B. Hancock, B. James and J. Curtis, "A Numerical Study of Granular Shear Flows of Rod-Like Particles Using the Discrete Element Method," J. Fluid. Mech. **713**, 1 (2012).

[4] Y. Guo, C. Wassgren, B. Hancock, W. Ketterhagen and J. Curtis, "Granular Shear Flows of Flat Disks and Elongated Rods Without and With Friction," Physics of Fluids **25**, 063304 (2013).

[5] T. Börzsönyi, B. Szabó, G. Törös, S. Wegner, J. Török, E. Somfai, T. Bien and R. Stannarius, "Orientational Order and Alignment of Elongated Particles Induced by Shear," Phys. Rev. Lett. **108**, 228302 (2012).

[6] T. Börzsönyi, B. Szabó, S. Wegner, K. Harth, J. Török, E. Somfai, T. Bien and R. Stannarius, "Shear-Induced Alignment and Dynamics of Elongated Granular Particles," Phys. Rev. E **86**, 051304 (2012).

[7] S. Wegner, T. Börzsönyi, To. Bien, G. Rose, and R. Stannarius, "Alignment and dynamics of elongated cylinders under shear," Soft Matter **8**, 10950 (2012).

[8] S. Wegner, R. Stannarius, A. Boese, G. Rose, B. Szabó, E. Somfai, and T. Börzsönyi, "Effects of grain shape on packing and dilatancy of sheared granular materials," Soft Matter **10**, 5157 (2014).

[9] D. J. Evans and G. P. Morriss, *Statistical Mechanics of Non-equilibrium Liquids* (Academic, London, 1990).

[10] T. Marschall and S. Teitel, "Compression-driven jamming of athermal frictionless spherocylinders in two dimensions," Phys. Rev. E **97**, 012905 (2018).

[11] D. J. Durian, "Foam Mechanics at the Bubble Scale," Phys. Rev. Lett. 75, 4780 (1995) and "Bubble-scale model of foam mechanics: Melting, nonlinear behavior, and avalanches," Phys. Rev. E 55, 1739 (1997).

[12] T. A. Marschall, S. V. Franklin, and S. Teitel, "Compression- and shear-driven jamming of U-shaped particles in two dimensions," Granular Matter **17**, 121 (2015).

[13] Y.-E. Keta and P. Olsson, unpublished.

[14] D. Vågberg, P. Olsson, and S. Teitel, "Shear banding, discontinuous shear thickening, and rheological phase transitions in athermally sheared frictionless disks," Phys. Rev. E **95**, 052903 (2017).

[15] P. Olsson and S. Teitel, "Critical scaling of shearing rheology at the jamming transition of soft-core frictionless disks," Phys. Rev. E **83**, 030302(R) (2011).

[16] D. Vågberg, D. Valdez-Balderas, M. A. Moore, P. Olsson, and S. Teitel, "Finite-size scaling at the jamming transition: Corrections to scaling and the correlation-length critical exponent," Phys. Rev. E 83, 030303(R) (2011).

[17] P. Olsson and S. Teitel, "Herschel-Bulkley Shearing Rheology Near the Athermal Jamming Transition," Phys. Rev. Lett. **109**, 108001 (2012).

[18] P. Olsson, unpublished.

[19] See Supplemental Material.

[20] For spherocylinders it is somewhat ambiguous how to define the location of a contact when two flat sides are touching. Here we take such a contact to have unit strength but distribute its location evenly over the segments of the flat surfaces that are in contact. For small α our results are insensitive to this as compared to other choices.

[21] For 2D spherocylinders we find that, for $\dot{\gamma} \to 0$ in the dense region near and above $\phi_J^{(0)}$, the integrated probability for a contact to form anywhere along the flat sides appears to stay constant as $\alpha \to 0$, even though the length of the flat sides is vanishing.

[22] K. VanderWerf, W. Jin, M. D. Shattuck, and C. S. O'Hern, "Hypostatic jammed packings of frictionless nonspherical particles," Phys. Rev. E **97**, 012909 (2018).

Orientational Ordering in Athermally Sheared, Aspherical, Frictionless Particles
Supplemental Material

Our argument in the main text, that $\lim_{\alpha\to 0}[S_{2\,\max}] = S_0$ is finite, relied on the assertion that our data at the smallest $\alpha = 0.001$ are reliable. In order to argue conversely, i.e., that $S_{2\,\max}$ vanishes as a power law as $\alpha \to 0$, we would have to believe that the value of $S_{2\,\max}$ at $\alpha = 0.001$ that is reported in Fig. 4a of the main text is, by some artifact of our simulations, larger than it should be.

Here we provide several tests to support our claim that our data point at $\alpha = 0.001$ is indeed correct. Since our simulations for 2D spherocylinders are considerably less time consuming than for 3D ellipsoids, we can make more exacting tests for that case. Hence, here we restrict ourselves to 2D spherocylinders.

I. DEPENDENCE ON SHEAR STRAIN RATE

As shown in Fig. 1 of the main text, the nematic order parameter S_2 depends on both packing fraction ϕ and shear strain rate $\dot\gamma$. However at each ϕ, S_2 approaches a limiting value as $\dot\gamma$ decreases. Here we wish to confirm that we have simulated at small enough $\dot\gamma$ so that the peak value $S_{2\,\max}$ which we find for $\alpha = 0.001$ has reached this $\dot\gamma \to 0$ limit. In Fig. SM-1a we plot S_2 vs ϕ for our three smallest strain rates $\dot\gamma$, using a system with $N = 1024$ particles. Just as was found in Fig. 1 of the main text for a larger α, here we see $\dot\gamma$ dependence remaining on the large ϕ side of the peak in S_2, however there is no $\dot\gamma$ dependence on the low ϕ side up to, and including, the peak value. Thus our results of Fig. SM-1a clearly argue that the value of $S_{2\,\max}$ will not decrease if $\dot\gamma$ were made even smaller.

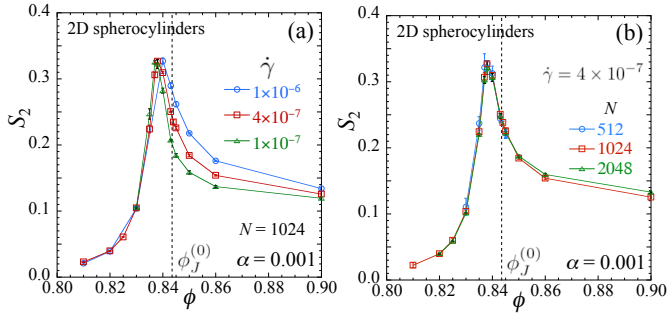

FIG. SM-1. Nematic order parameter S_2 for $\alpha = 0.001$ vs packing fraction ϕ for (a) three different shear strain rates $\dot\gamma$ with $N = 1024$ particles, and (b) systems with different numbers of particles N for $\dot\gamma = 4\times10^{-7}$. Vertical dashed lines locate the jamming transition of $\alpha = 0$ spherical particles, $\phi_J^{(0)} = 0.8433$.

II. DEPENDENCE ON SYSTEM SIZE

As one approaches the jamming transition, a correlation length diverges. If one is too close to the jamming transition, finite size effects may become important when the correlation length becomes larger than the length of the system. We thus wish to check that our value of $S_{2\,\max}$ for $\alpha = 0.001$ is not affected by such possible finite system size effects. Our results in the main text are for systems with $N = 1024$ particles. In Fig. SM-1b we plot S_2 vs ϕ at the small strain rate $\dot\gamma = 4\times10^{-7}$, using three different systems sizes with numbers of particles $N = 512, 1024$ and 2048. While there is a small dependence on N seen at the largest ϕ, there is no dependence on N at lower ϕ up to and including the peak value. Our value of $S_{2\,\max}$ for $\alpha = 0.001$ thus does not suffer from finite size effects.

III. DEPENDENCE ON INTEGRATION TIME STEP

We should also check if there is any dependance of our results on the size of the finite numerical integration step Δt. Our results in the main text used a value $\Delta t = 0.02 t_0$ with $t_0 = D_s^2 k_d/k_e$ the unit of time. In Fig. SM-2 we plot S_2 vs ϕ at the small strain rate $\dot\gamma = 4\times10^{-7}$, for $\alpha = 0.001$, using three different values of the time step $\Delta t/t_0 = 0.01, 0.02$ and 0.04. We see that any differences between the data from the three different Δt are within the estimated statistical error. We conclude that our integration step of $\Delta t/t_0 = 0.02$ is small enough to accurately determine $S_{2\,\max}$ for $\alpha = 0.001$.

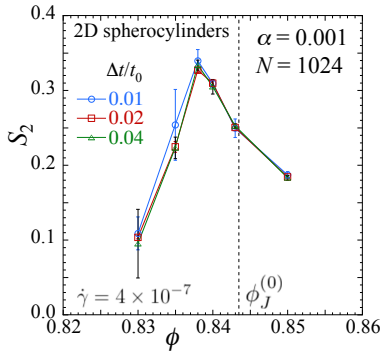

FIG. SM-2. Nematic order parameter S_2 for $\alpha = 0.001$ vs packing fraction ϕ using different integration time steps $\Delta t/t_0 = 0.01, 0.02$ and 0.04. The system is sheared at a strain rate $\dot\gamma = 4\times10^{-7}$ and has $N = 1024$ particles. Vertical dashed line locates the jamming transition of $\alpha = 0$ spherical particles, $\phi_J^{(0)} = 0.8433$.

IV. EQUILIBRATION

Finally we demonstrate that the rotational degrees of freedom in our system are well equilibrated for our simulations at $\alpha = 0.001$. When α is small, the small moment arms of the collisional forces result in small torques, and, depending on the particle density, it can require long shear strains for the rotational degrees of freedom of the system to equilibrate to the proper steady state.

Let us define $S_2(\gamma)$ as the magnitude of the instantaneous nematic order parameter of the individual configuration of the system after it has sheared a strain $\gamma = \dot{\gamma}t$. For an initial configuration of randomly oriented particles, a system with a finite number of particles N will have some initial value $S_2(0)$. At low densities, where torque inducing collisions are rare, particles will rotate primarily under the influence of the dissipative torque. In this case, since particles with finite α have a non uniform angular velocity that depends on their orientation θ_i, the relative orientations of the particle spines $\hat{\boldsymbol{\ell}}_i$ will vary with γ and hence so will S_2. But once the system has strained so that $\gamma = \dot{\gamma}T$, where T is the period of rotation of an isolated particle, the particles will have returned to their initial orientations and $S_2(\gamma)$ will have returned to its initial value $S_2(0)$. We thus expect to see an oscillating $S_2(\gamma)$ with period $\dot{\gamma}T$. We have observed such behavior for small α at low densities. However, as the density increases the rate of collisions increases. These collisions will perturb this oscillatory behavior until, after a sufficiently large strain has been applied, the particle orientations have lost memory of their initial configuration. The particle orientations will then sample a stationary steady state distribution. $S_2(\gamma)$ will then be constant, aside from random fluctuations that we might expect should decrease as $1/\sqrt{N}$ as the number of particles N increases.

In Fig. SM-3a we plot $S_2(\gamma)$ vs γ for a shear strain rate $\dot{\gamma} = 4 \times 10^{-7}$ at a packing $\phi = 0.838$ near the peak in S_2, for a system with $N = 1024$ particles with $\alpha = 0.001$. We see that $S_2(\gamma)$ appears, as desired, to consist of random fluctuations about a constant average. The dashed horizontal line in Fig. SM-3a is the average $\langle S_2(\gamma)\rangle = (1/\Delta\gamma)\int_{\gamma_i}^{\gamma_f} d\gamma\, S_2(\gamma)$, where $\Delta\gamma = \gamma_f - \gamma_i$; we start averaging only after an initial shear strain of $\gamma_i = 10$ so as to avoid any initial transients, and average up to a final $\gamma_f = 150$. The solid horizontal line represents the ensemble average S_2, as considered elsewhere in this work. To be clear, $S_2(\gamma)$ is the largest eigenvalue of the orientational ordering tensor $T_{\mu\nu}(\gamma)$ as computed for the individual configuration at strain γ, while S_2 is the largest eigenvalue of the orientational ordering tensor $\langle T_{\mu\nu}\rangle$ averaged over the length of the shearing run from γ_1 to γ_2. Since the relation between eigenvalue and tensor is not linear, these two averages of S_2 need not be equal, and in Fig. SM-3a we see that there is indeed a small difference. Since the direction of the nematic director is optimized to give the largest possible S_2, and since the direction of the nematic director obtained from $T_{\mu\nu}(\gamma)$ fluctuates as γ varies from configuration to configuration (as opposed to the director obtained from $\langle T_{\mu\nu}\rangle$ which is fixed), we expect that $\langle S_2(\gamma)\rangle$ will be somewhat larger than S_2, and this is indeed what is observed in Fig. SM-3a. In Fig. SM-3b we plot $\langle S_2(\gamma)\rangle - S_2$ vs N and see that this difference is going to zero as N increases. In the same figure we also plot the standard deviation $\sigma_{S_2(\gamma)} = \sqrt{\langle S_2^2(\gamma)\rangle - \langle S_2(\gamma)\rangle^2}$ vs N and see that it also vanishes as N increases.

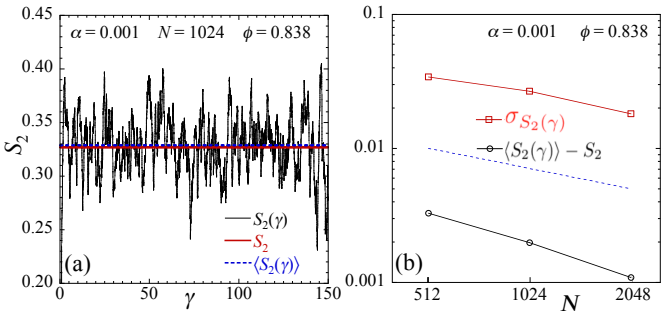

FIG. SM-3. (a) Instantaneous nematic order parameter $S_2(\gamma)$ vs shear strain γ, for $\alpha = 0.001$ and shear strain rate $\dot{\gamma} = 4 \times 10^{-7}$ at packing fraction $\phi = 0.838$ near the peak value $S_{2\,\max}$. The horizontal dashed line is the average over these instantaneous values $\langle S_2(\gamma)\rangle$, while the horizontal solid line is S_2 as obtained from averaging the orientational ordering tensor over the entire shearing run. The system has $N = 1024$ particles. (b) Difference $\langle S_2(\gamma)\rangle - S_2$ vs number of particles N, and standard deviation $\sigma_{S_2(\gamma)}$ vs N; the dashed line is $\sim 1/\sqrt{N}$ for comparison.

Next, we consider the Fourier transform of $S_2(\gamma)$ in order to check that the frequency spectrum of the fluctuating noise seen in Fig. SM-3a is broad without any peaks that could indicate vestigial oscillations due to poor equilibration. Since $S_2(\gamma)$ is plotted in terms of the dimensionless time $\gamma = \dot{\gamma}t$, in Fig. SM-4 we plot the Fourier transform $\mathcal{F}[S_2]$ as a function of the dimensionless frequency $\omega/\dot{\gamma}$. We see that the spectrum is indeed broad with no peaks. The high frequency tail is roughly power law with an exponent 1.3, however that exponent changes a bit depending on the range of γ that is used in the fit.

Lastly we consider a similar analysis of the orientation angle θ_2 of the nematic director. In Fig. SM-5a we plot the instantaneous $\theta_2(\gamma)$ vs γ for the same parameters as in Fig. SM-3a, $\dot{\gamma} = 4 \times 10^{-7}$, $\phi = 0.838$, $\alpha = 0.001$. We see what appear to be random fluctuations about a constant average value. The dashed horizontal line is the average $\langle\theta_2(\gamma)\rangle = (1/\Delta\gamma)\int_{\gamma_i}^{\gamma_f} d\gamma\,\theta_2(\gamma)$, while the solid horizontal line is θ_2 obtained from the ensemble averaged orientation tensor $\langle T_{\mu\nu}\rangle$. In Fig. SM-5b we plot the Fourier transform $\mathcal{F}[\theta_2]$ vs the dimensionless frequency $\omega/\dot{\gamma}$. We see a broad spectrum with a power law tail decreasing with an exponent ~ 1.5 (the exact value of this exponent is sensitive to the range of data used in the fit). There are no peaks in $\mathcal{F}[\theta_2]$ to indicate any oscillatory

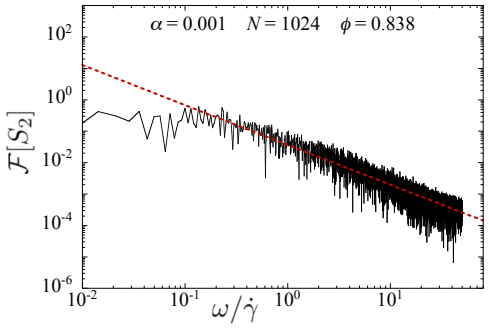

FIG. SM-4. Fourier transform of $S_2(\gamma)$, $\mathcal{F}[S_2]$, vs dimensionless frequency $\omega/\dot{\gamma}$. The high frequency tail is fit to an inverse power law (dashed line) and gives an exponent ~ 1.3.

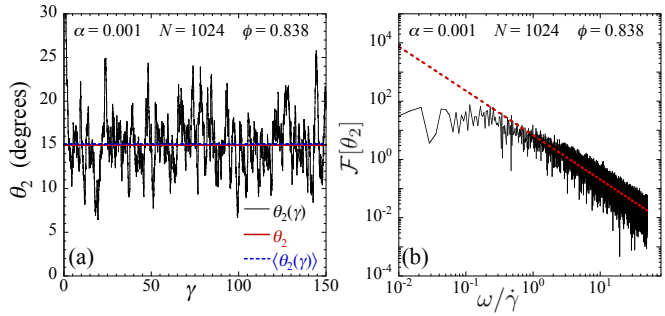

FIG. SM-5. (a) Instantaneous nematic director angle $\theta_2(\gamma)$ vs shear strain γ, for $\alpha = 0.001$ and shear strain rate $\dot{\gamma} = 4\times10^{-7}$ at packing fraction $\phi = 0.838$ near the peak value $S_{2\,\mathrm{max}}$. The horizontal dashed line is the average over these instantaneous values $\langle\theta_2(\gamma)\rangle$, while the horizontal solid line is θ_2 as obtained from averaging the orientational ordering tensor over the entire shearing run. The system has $N = 1024$ particles. (b) Fourier transform of $\theta_2(\gamma)$, $\mathcal{F}[\theta_2]$, vs dimensionless frequency $\omega/\dot{\gamma}$. The high frequency tail is fit to an inverse power law (dashed line) and gives an exponent ~ 1.5.

motion, thus giving support to the assertion in the main text that, while individual particles tumble with an average angular velocity $\langle\omega_i\rangle$, there is no coherent tumbling of the nematic order parameter $\mathbf{S}_2$. Our results in this section thus confirm that our spherocylinder simulations at $\alpha = 0.001$ are indeed well equilibrated.